



# Highly dispersed $\text{Pt}^{\delta+}$ on $\text{Ti}_x\text{Ce}_{(1-x)}\text{O}_2$ as an active phase in preferential oxidation of CO



S. Rico-Francés<sup>a</sup>, E.O. Jardim<sup>a</sup>, T.A. Wezendonk<sup>b</sup>, F. Kapteijn<sup>b</sup>, J. Gascon<sup>b</sup>,  
A. Sepúlveda-Escribano<sup>a</sup>, Enrique V. Ramos-Fernandez<sup>a,\*</sup>

<sup>a</sup> Laboratorio de Materiales Avanzados, Departamento de Química Inorgánica – Instituto Universitario de Materiales de Alicante, Universidad de Alicante, Apartado 99, E-03080 Alicante, Spain

<sup>b</sup> Catalysis Engineering, Chemical Engineering Department, Delft University of Technology, Julianalaan 136, 2628 BL Delft, The Netherlands

## ARTICLE INFO

### Article history:

Received 18 March 2015

Received in revised form 18 May 2015

Accepted 16 June 2015

Available online 20 June 2015

### Keywords:

PROX

Ceria

Titania

Platinum

Hydrogen purification

## ABSTRACT

Structure–activity relationships for 1 wt.% Pt catalysts were investigated for a series of  $\text{Ti}_x\text{Ce}_{(1-x)}\text{O}_2$  ( $x = 1, 0.98, 0.9, 0.5, 0.2$  and  $0$ ) supports prepared by the sol–gel method. The catalysts prepared by impregnation were characterized in detail by applying a wide range of techniques as  $\text{N}_2$ -isotherms, XRF, XRD, Raman, XPS,  $\text{H}_2$ -TPR, Drifts, UV–vis, etc. and tested in the preferential oxidation of CO in the presence of  $\text{H}_2$ . Also several reaction conditions were deeply analyzed. A strong correlation between catalyst performance and the electronic properties let us to propose, based in all the experimental results, a plausible reaction mechanism where several redox cycles are involved.

© 2015 Elsevier B.V. All rights reserved.

## 1. Introduction

Hydrogen production and purification are two processes of great interest nowadays. On the one hand, hydrogen is used in large amounts in refineries and considered as a green energy carrier. When used as fuel in Proton Exchange Membrane Fuel Cells (PEMFC) electricity can be produced in a very efficient manner. On the other hand, hydrogen is typically produced by steam reforming of methane. After the steam reforming unit, the stream contains elevated CO amounts that need to be reduced below 10 ppm, which is the maximum tolerable level for platinum electrodes used in PEMFC. The first purification step is carried out by a two-step Water Gas Shift (WGS) process, at high and at low temperature; however, the remaining CO concentration is still above the tolerable level for PEMFC. Therefore, further purification is required. Several options compete for CO removal: membranes, methanation and preferential oxidation to  $\text{CO}_2$ , the latter being the most promising one [1,2].

An efficient catalyst for the PROX reaction should convert CO to  $\text{CO}_2$  and should not promote the competing oxidation of  $\text{H}_2$ . Indeed, such an ideal catalyst should convert CO molecules in the pres-

ence of an excess of  $\text{H}_2$ , together with other components that can negatively affect the activity, like  $\text{H}_2\text{O}$  or  $\text{CO}_2$ .

Cerium oxide has been proven as an efficient catalyst support to be used for this reaction. Mechanistic studies have shown that the oxygen lattice plays an important role in the reaction, since it follows a Mars van Krevelen mechanism [3]. It means that CO is chemisorbed on the Pt nanoparticles and oxygen is supplied by the support, generating reduced Ce(III) cations that are oxidized back with oxygen from the feed. In this way, the support plays a vital role in the reaction. It is well known that the incorporation of a second metal in the  $\text{CeO}_2$  lattice can enhance ceria reducibility.  $\text{ZrO}_2$  oxide is the most studied dopant by far, as it can increase the oxide reducibility over an order of magnitude [4,5]. However,  $\text{ZrO}_2$  is very inert and cannot be reduced even at high temperatures in the presence of  $\text{H}_2$ . It means that part of the mixed metal support ( $\text{ZrO}_2$ – $\text{CeO}_2$ ) is not reducible. Based on our knowledge about doped ceria, in this work we present the use of  $\text{TiO}_2$ – $\text{CeO}_2$  solid solutions as supports; a mixture of reducible oxides ( $\text{Ti}^{4+}$  and  $\text{Ce}^{4+}$ ) will eventually improve the performance. If both oxides synergistically participate in the Mars van Krevelen mechanism, an improve of catalytic performance might be produced.

\* Corresponding author. Tel.: +34 96 590 9350; fax: +34 965909820.

E-mail address: [Enrique.ramos@ua.es](mailto:Enrique.ramos@ua.es) (E.V. Ramos-Fernandez).

**Table 1**  
Chemical composition of the Pt/Ti<sub>x</sub>Ce<sub>(1-x)</sub>O<sub>2</sub> catalysts, with  $x = 1, 0.98, 0.9, 0.5, 0.2$  and  $0$ .

	Ti content, (at.%)	Ce content, (at.%)	Pt dispersion <sup>a</sup> (%)	TOF (60 °C) s <sup>-1</sup>
Pt/TiO <sub>2</sub>	100	0	12.6	0.0259
Pt/Ti <sub>0.98</sub> Ce <sub>0.02</sub> O <sub>2</sub>	97	3	58.2	0.0393
Pt/Ti <sub>0.9</sub> Ce <sub>0.1</sub> O <sub>2</sub>	84	16	78.1	0.0546
Pt/Ti <sub>0.5</sub> Ce <sub>0.5</sub> O <sub>2</sub>	55	45	85.3	0.0661
Pt/Ti <sub>0.2</sub> Ce <sub>0.8</sub> O <sub>2</sub>	20	80	75.7	0.0242
Pt/CeO <sub>2</sub>	0	100	58.9	0.0058

<sup>a</sup> Calculated by CO chemisorption, assuming 1CO:1Pt stoichiometry.

## 2. Experimental

### 2.1. Synthesis of supports and catalysts

Ti<sub>x</sub>Ce<sub>(1-x)</sub>O<sub>2</sub> supports with different molar compositions ( $x = 1, 0.98, 0.9, 0.5, 0.2$  and  $0$ ), were synthesized using the sol–gel method [6]. The proper amount of cerium nitrate (Ce(NO<sub>3</sub>)<sub>3</sub>·6H<sub>2</sub>O, 99.00% Aldrich) was dissolved in an aqueous HNO<sub>3</sub> solution (0.02 M) contained in a round bottom flask. Then, titanium iso-propoxide (Ti[OCH(CH<sub>3</sub>)<sub>2</sub>]<sub>4</sub>, 97.00% Aldrich) was added drop-wise under continuous stirring. A white precipitate appeared. The suspension was heated for 30 min at 80 °C under stirring. In this step, a fraction of the alcohol formed after alkoxide hydrolysis was evaporated. In order to obtain a complete gelification, the suspension was refluxed at 80 °C for two hours. The gel obtained was dried in an oven at 40 °C for 8 days. Pure TiO<sub>2</sub> was prepared following the same procedure, using only titanium precursor. Furthermore, pure CeO<sub>2</sub> support was prepared by homogeneous precipitation with the same cerium precursor and urea (Fluka, 98%) dissolved in ultrapure water. The mixture was heated at 90 °C with constant stirring during 11 h. At the end, ammonia solution was added drop-wise to complete precipitation. The solid was separated by filtration and washed with ultrapure water. Finally, the solids prepared were calcined at 500 °C for 5 h, with a heating rate of 2 °C min<sup>-1</sup>.

For catalysts preparation, the supports were impregnated with an aqueous solution of the platinum precursor (H<sub>2</sub>PtCl<sub>6</sub>·6H<sub>2</sub>O, Alfa Aesar 99.90%, 10 ml g<sup>-1</sup> support) of the adequate concentration to load 1 wt.% Pt. The slurry was stirred for 12 h at room temperature in a rotary evaporator, and then the solvent was removed under vacuum at 70 °C. After drying, the solids were calcined at 500 °C for 2 h, with a heating rate of 3 °C min<sup>-1</sup>.

### 2.2. Characterization of supports and catalysts

The composition of the supports was determined by X-Ray fluorescence (XRF). An X-Ray sequential spectrometer (PHILIPS MAGIX PRO) equipped with a rhodium X-ray tube and beryllium window was used. The textural properties of the supports were characterized by N<sub>2</sub> adsorption–desorption measurements at –196 °C. Gas adsorption experiments were performed in homemade fully automated manometric equipment. Prior to the adsorption experiments, samples were out-gassed at 250 °C for 4 h under vacuum (10<sup>-4</sup> Pa). The “apparent” surface area was estimated after application of the BET equation.

X-ray powder diffraction patterns were recorded on a Bruker D8-Advance system with a Göebel mirror and a Kristalloflex K 760-80 F X-Ray generator, fitted with a Cu cathode and a Ni filter. Diffractograms were registered between 20 and 80° (2θ) with a step of 0.1° and a time per step of 3 s.

X-ray photoelectron spectroscopy (XPS, K-ALPHA, Thermo Scientific) was used to analyze the catalysts surface. All spectra were collected using Al-K radiation (1486.6 eV), monochromatized by a twin crystal monochromator, yielding a focused X-ray spot with a diameter of 400 μm, at 3 mA × 12 kV. The alpha hemispherical analyzer was operated in the constant energy mode with survey

scan pass energies of 200 eV to measure the whole energy band and 50 eV in a narrow scan to selectively measure the particular elements. Thus, XPS was used to assess the chemical bonding state as well as the elemental composition of the sample surface. Charge compensation was achieved with the system flood gun that provides low energy electrons and low energy argon ions from a single source. The intensities were estimated by calculating the integral of each peak, after subtraction of the S-shaped background and by fitting the experimental curve to a combination of a Lorentzian (30%) and Gaussian (70%) lines [7]. All binding energies (BE) were referenced to the C 1s line at 284.6 eV, which provided binding energy values with an accuracy of ±0.2 eV. The surface atomic ratios were estimated from the integrated intensities corrected by the atomic sensitivity factors.

Temperature-programmed reduction with H<sub>2</sub> (H<sub>2</sub>-TPR) experiments were carried out in a U-shaped quartz cell reactor using a 5% H<sub>2</sub>/He gas flow of 50 cm<sup>3</sup> min<sup>-1</sup>, with a heating rate of 10 °C min<sup>-1</sup>. Previous to the TPR run, the samples (100 mg) were treated with flowing 50 cm<sup>3</sup> min<sup>-1</sup> of He at 150 °C for 2 h. Hydrogen consumption was followed by on-line mass spectrometry calibrated by carrying out the reduction of CuO and assuming complete reduction to metallic copper.

Raman spectra were recorded on a LabRam spectrometer (Jobin-Yvon Horiba) coupled to an Olympus microscope with a lens of 50×/0.5LMPlanFI. He/Ne laser excitation source (633 nm) was used, and the spectrometer resolution in these conditions was 3 cm<sup>-1</sup>. The wavelength was calibrated using Si signal at 520 cm<sup>-1</sup>.

The UV–vis spectroscopy analysis was carried out in a Jasco V-650, a double-beam spectrophotometer with a photomultiplier tube detector. The high sensitivity of the photomultiplier tube detector enables accurate measurements of low concentration samples. The accessory used for measure the solid samples is an integrating sphere ISV-722 UV–vis. Spectra were taken in the wavelength range of 200–800 nm (scan speed 400 nm min<sup>-1</sup> and data interval of 1 nm).

Nicolet 6700 FT-IR (Thermo Scientific) spectrometer equipped with MCT-A detector and high-temperature DRIFTS cell (spectral resolution 4 cm<sup>-1</sup>) was used to study CO adsorption on the catalyst, obtaining information about Pt coordination and electronic structure. Spectra were recorded at room temperature after calcinations in air at 500 °C followed by a reduction with H<sub>2</sub> flow at 250 °C and CO adsorption (0.5% and 1% CO flow until saturation) at 25 °C. After flushing with He (50 cm<sup>3</sup> min<sup>-1</sup>), temperature was increased and spectra were taken every 50 °C until achieving 500 °C. Each reported spectrum is an average of 280 scans.

CO chemisorption studies were carried out in the Micromeritics ASAP 2020C system. The purity of all gases used was greater than 99.999%. In a typical analysis, 0.3–0.4 g of sample was pretreated in flowing He at 120 °C for 2 h, followed by evacuation at 120 °C. Afterwards, the sample was reduced in-situ by flowing H<sub>2</sub> at 250 °C for 1 h. This temperature was maintained during evacuation at 5 Pa for 2 h. The sample was subsequently cooled down to the analysis temperature of 35 °C. The ramp rate for heating and cooling was fixed at 5 °C min<sup>-1</sup>. Adsorption measurements were carried out at partial CO pressures from 80 to 600 Torr. First, the total CO adsorption

was obtained after the sample was evacuated at analysis temperature for 1 h. Second, the reversible adsorption was obtained in the following measurement. The difference between the first and second measurement is the irreversible adsorption (strong monolayer chemisorption). Pt dispersion was estimated by extrapolating the total gas uptake from the near-constant linear difference curve at zero pressure.

### 2.3. Catalytic activity tests

Catalytic activity measurements for the PROX reaction were carried out in a U-shaped quartz fixed-bed reactor containing 100 mg of the catalyst. Previous to the reaction, samples were reduced in-situ using hydrogen flow ( $50 \text{ cm}^3 \text{ min}^{-1}$ ) at  $250^\circ\text{C}$  with a heating rate of  $5^\circ\text{C min}^{-1}$ . The PROX reaction was studied in the temperature range  $30\text{--}200^\circ\text{C}$  and atmospheric pressure, with a gas mixture containing 20–70%  $\text{H}_2$ , 2%  $\text{CO}$ , 2%  $\text{O}_2$ , 5%  $\text{CO}_2$ , 5%  $\text{H}_2\text{O}$  and He as a balance (total flow:  $50 \text{ cm}^3 \text{ min}^{-1}$ ; GHSV:  $17000 \text{ h}^{-1}$ ). Reaction products were analyzed by on-line gas chromatography (coupled with FID and TCD detectors), using a Plot/Q and a Molesieve capillary column to separate the reactants and the products. Carbon monoxide and oxygen conversion, selectivity toward  $\text{CO}_2$  and yield were estimated based on the follow equations (being  $n_{\text{in}}$  the moles introduced in the reactor and  $n_{\text{out}}$  the ones at the exit, after reaction):

$$X_{\text{CO}} = \frac{n_{\text{CO}}^{\text{in}} - n_{\text{CO}}^{\text{out}}}{n_{\text{CO}}^{\text{in}}} \times 100 \quad (1)$$

$$X_{\text{O}_2} = \frac{n_{\text{O}_2}^{\text{in}} - n_{\text{O}_2}^{\text{out}}}{n_{\text{O}_2}^{\text{in}}} \times 100 \quad (2)$$

$$S_{\text{CO}_2} = \frac{1}{2} \frac{n_{\text{CO}}^{\text{in}} - n_{\text{CO}}^{\text{out}}}{n_{\text{O}_2}^{\text{in}} - n_{\text{O}_2}^{\text{out}}} \times 100 \quad (3)$$

$$\text{Yield}_{\text{CO}_2} = \frac{X_{\text{O}_2} S_{\text{CO}_2}}{100} = \frac{1}{2} \frac{n_{\text{CO}}^{\text{in}} - n_{\text{CO}}^{\text{out}}}{n_{\text{O}_2}^{\text{in}}} \times 100 \quad (4)$$

For calculating catalyst activity in terms of *Turn Over Frequency*, Eq. (5) was used. This one relates the converted moles ( $\text{mmol CO}_{\text{trans}}$ ) per time unit with the superficial metal ( $\text{mmol Pt}_{\text{surf}}$ ); calculated based on weight percentage and dispersion values.

$$\text{TOF} = \frac{\text{mmol CO}_{\text{trans}} \cdot \text{s}^{-1}}{\text{mmol Pt}_{\text{surf}}} \quad (5)$$

## 3. Results

### 3.1. Chemical and textural properties

Table 1 reports the chemical composition of supports and catalysts. The series ranges from pure  $\text{TiO}_2$  to pure  $\text{CeO}_2$ . The majority of the experimental compositions of the supports determined by XRF are similar to the nominal ones except for  $x = 0.9$ , which is slightly

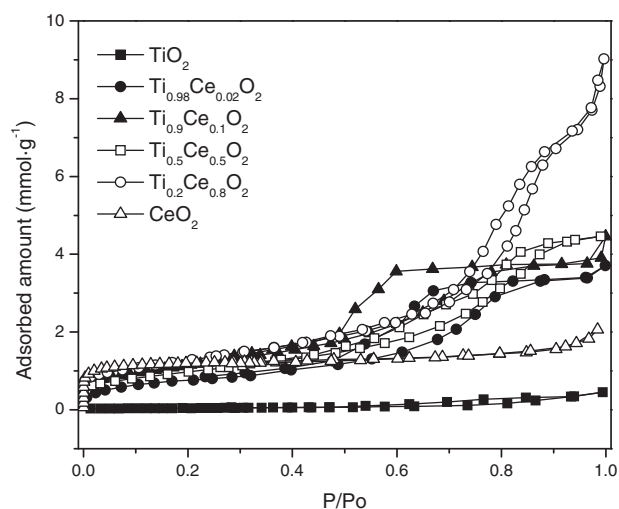


Fig. 1.  $\text{N}_2$  adsorption-desorption isotherms at  $-196^\circ\text{C}$  for the supports.

Table 2  
Textural properties of the  $\text{Ti}_x\text{Ce}_{1-x}\text{O}_2$  supports.

	$S_{\text{BET}}$ ( $\text{m}^2 \text{ g}^{-1}$ )	$V_{\text{T}}$ ( $\text{cm}^3 \text{ g}^{-1}$ )	$V_0$ ( $\text{cm}^3 \text{ g}^{-1}$ )	$V_{\text{meso}}$ ( $\text{cm}^3 \text{ g}^{-1}$ )
$\text{TiO}_2$	<10	0.02	0.00	0.02
$\text{Ti}_{0.98}\text{Ce}_{0.02}\text{O}_2$	60	0.13	0.02	0.11
$\text{Ti}_{0.9}\text{Ce}_{0.1}\text{O}_2$	70	0.13	0.03	0.10
$\text{Ti}_{0.5}\text{Ce}_{0.5}\text{O}_2$	80	0.16	0.03	0.13
$\text{Ti}_{0.2}\text{Ce}_{0.8}\text{O}_2$	100	0.32	0.04	0.28
$\text{CeO}_2$	100	0.07	0.04	0.03
$\text{Pt/Ti}_{0.5}\text{Ce}_{0.5}\text{O}_2^{\text{a}}$	70	0.16	0.03	0.13
$\text{Pt/TiO}_2^{\text{b}}$	< 10	0.04	0.00	0.04
$\text{Pt/Ti}_{0.2}\text{Ce}_{0.8}\text{O}_2^{\text{b}}$	70	0.28	0.03	0.25

$V_{\text{T}}$  calculated at  $P/P_0 = 0.99$ .  $V_0$  and  $V_{\text{meso}}$ : microporous and mesoporous volumes calculated using Dubinin-Radushkevich method.

<sup>a</sup> Fresh catalysts.

<sup>b</sup> Used catalysts.

smaller. In this way, all the supports were labelled using the nominal composition.  $\text{N}_2$  adsorption-desorption isotherms at  $-196^\circ\text{C}$  for the different supports are plotted in Fig. 1; whereas the isotherm for pure  $\text{TiO}_2$  is typical of a non porous solid, the isotherms for the Ce-containing supports are Type IV according to the IUPAC classification, which is typical for mesoporous solids, and they exhibit Type H1 hysteresis loops. Table 2 shows the textural properties of all the samples, obtained from the  $\text{N}_2$  isotherms. It can be seen that, as expected, the pure titania support presents a very low surface area. In contrast, ceria addition produces a very important increase in surface area, reaching  $100 \text{ m}^2 \text{ g}^{-1}$  for the sample with the highest ceria content, comparable to that of the pure ceria support. Several isotherms for catalysts before and after reaction were also measured (not shown). Platinum addition does not affect the surface area; however, a small decrease in the surface was observed for used catalysts (Table 2).

Table 3  
Crystallite size, lattice constants and phase transformation percentage obtained from XRD patterns.

	$\text{TiO}_2$ (anatase)			$\text{CeO}_2$ (fluorite)	
	Crystallite size $D$ (nm)	Peak (1 0 1) $2\theta$	Phase transf. $f_{\text{R}}$ (%)	Crystallite size $D$ (nm)	Peak (1 1 1) $2\theta$
$\text{TiO}_2$	20	25.3	45	—	—
$\text{Ti}_{0.98}\text{Ce}_{0.02}\text{O}_2$	5	25.3		—	—
$\text{Ti}_{0.9}\text{Ce}_{0.1}\text{O}_2$	6	25.4		—	—
$\text{Ti}_{0.5}\text{Ce}_{0.5}\text{O}_2$	—	—		7	28.7
$\text{Ti}_{0.2}\text{Ce}_{0.8}\text{O}_2$	—	—		8	28.6
$\text{CeO}_2$	—	—		14	28.5

### 3.2. X-Ray diffraction

Fig. 2 shows the XRD patterns for the different supports after calcination. For pure titania, the characteristic peaks of the anatase and the rutile phases are clearly evidenced with a slightly larger proportion of anatase. On the other hand, the brookite phase has not been detected in any case [8–10]. The intensity of the anatase characteristic peaks decreases when the amount of cerium increases, also a small broadening along with a slight shift toward larger angles (see Table 3) is observed for these characteristic reflections. In the XRD pattern of support  $\text{Ti}_{0.5}\text{Ce}_{0.5}\text{O}_2$  the characteristic peaks of titania are hardly discernible, but those of the fluorite-type phase of ceria become evident [11,12]. Focusing in the X-ray diffractograms of supports with  $x=0.98$  and  $0.9$ , a new broad reflection appears at  $30.7^\circ$ . Table 3 shows the average crystal size of both titania and ceria, and it can be seen that the addition of ceria results in a decrease in crystal size of  $\text{TiO}_2$  while ceria crystal size increases with ceria content.

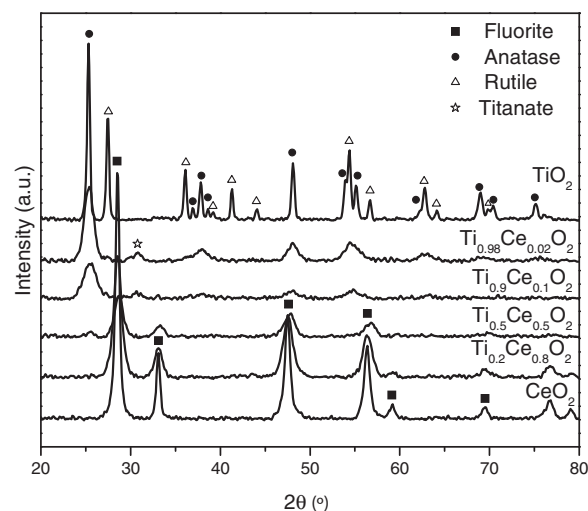


Fig. 2. X-ray diffraction patterns of  $\text{Ti}_x\text{Ce}_{(1-x)}\text{O}_2$  supports.

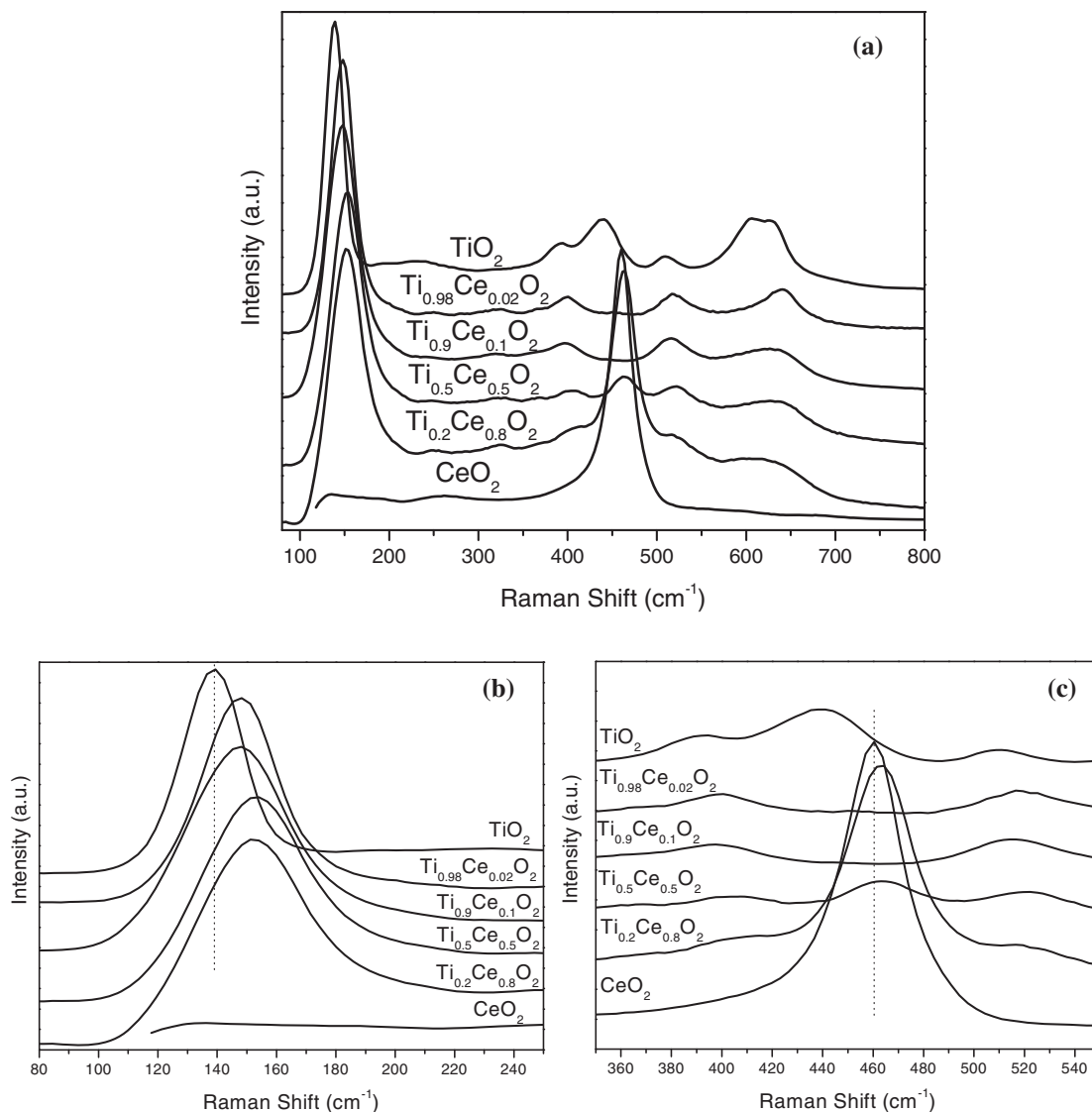


Fig. 3. Raman spectra of synthesized supports (a) and a zoom view of  $E_g$  mode for titania (b) and  $F_{2g}$  mode for ceria (c).

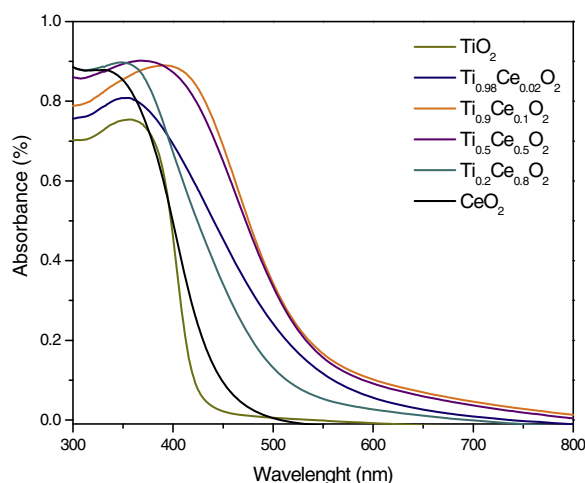


Fig. 4. UV-vis spectra for the supports.

### 3.3. Raman spectroscopy

Raman spectroscopy has been used to gain more information about possible amorphous phases present on the supports. Fig. 3(a) shows the Raman spectra of the different supports. For pure titania, the most intense band for anatase (O–Ti–O bonding type vibration;  $E_g$  144  $\text{cm}^{-1}$ ) and the other anatase features: 399 ( $B_{1g}$ ), 513 ( $A_{1g}$ ), 519 ( $B_{1g}$ ) and 639  $\text{cm}^{-1}$  ( $E_g$ ) [13] can be observed. In the case of rutile, its fundamental modes can be discerned at 143 ( $B_{1g}$ ), 447 ( $E_g$ ), 612 ( $A_{1g}$ ) [14]. As cerium is added, the anatase  $\text{TiO}_2$  peaks decrease, leading to the appearance of the symmetric breathing mode of cerium ( $F_{2g}$  ~ 464  $\text{cm}^{-1}$ ) for supports with high ceria content [15,16].

Furthermore, the  $E_g$   $\text{TiO}_2$  active mode shifts toward higher wavenumber values and also suffers a change in its symmetry and broadness (Fig. 3(b)). As it can be seen,  $\text{TiO}_2$  can be detected in all samples by its Raman active mode, contrary to what happens in the XRD spectra. The Raman spectrum of pure ceria exhibits a main peak at 462.9  $\text{cm}^{-1}$ , which is assigned to  $F_{2g}$  mode due to symmetrical stretching of Ce–O vibrational unit in eightfold coordination. It is interesting to note the decrease in intensity of this band with an increase of the titania content (Fig. 3(c)).

### 3.4. UV-vis

Fig. 4 shows the UV-vis spectra for all the samples. Both  $\text{TiO}_2$  and  $\text{CeO}_2$  have comparable UV-vis spectra. The increase in ceria concentration shifts the absorption band toward visible light up to a certain concentration,  $x=0.5$  then, the band again shifts to lower wavenumbers.

### 3.5. Temperature-programmed reduction

The reducibility of the catalysts was studied by mean of  $\text{H}_2$ -temperature-programmed reduction experiments. Fig. 5 shows the obtained reduction profiles: catalyst with the pure  $\text{TiO}_2$  support

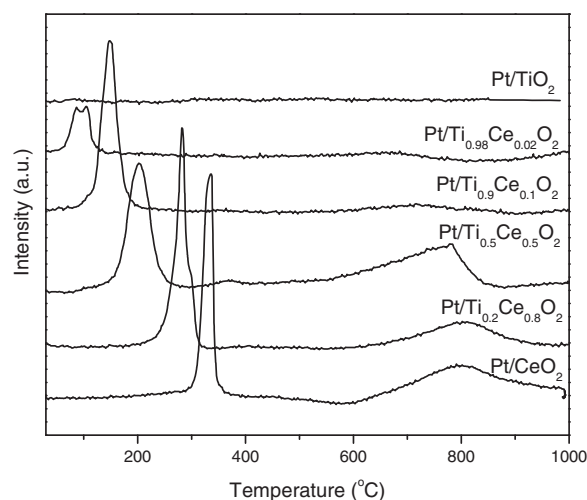
Fig. 5.  $\text{H}_2$ -TPR profiles for catalysts.

Table 4

Hydrogen consumption values for the first reduction peak of TPR profiles.

Catalysts	mmol $\text{H}_2$ g $^{-1}$
Pt/ $\text{TiO}_2$	0.025
Pt/ $\text{Ti}_{0.98}\text{Ce}_{0.02}\text{O}_2$	0.194
Pt/ $\text{Ti}_{0.9}\text{Ce}_{0.1}\text{O}_2$	0.567
Pt/ $\text{Ti}_{0.5}\text{Ce}_{0.5}\text{O}_2$	0.575
Pt/ $\text{Ti}_{0.2}\text{Ce}_{0.8}\text{O}_2$	0.574
Pt/ $\text{CeO}_2$	0.520

does not show any hydrogen consumption peak in the range of temperatures studied. When ceria is added to the support a reduction peak at low temperature (<400 °C) is observed. This peak shifts to higher temperature when ceria is added. Table 4 shows the quantification of hydrogen consumption in the TPR experiments, with a clear correlation between hydrogen consumption and ceria content up to  $x=0.5$ . Higher amounts of ceria result in a (relatively) lower  $\text{H}_2$  consumption.

### 3.6. X-ray photoelectron spectroscopy

The surface composition of all the catalysts after reduction at 250 °C was analyzed by means of XPS (all the graphs are shown in the supporting information). Fig. S2 shows the Ti 2 $p_{3/2}$  core level spectra of the catalysts after being reduced at 250 °C. The binding energy for Ti 2 $p_{3/2}$  in pure titania sample is centered at 459.3 eV (Table 5), which corresponds to  $\text{Ti}^{4+}$  [17]. The addition of cerium produces a shifting of this peak toward lower binding energies, reaching a value of 458.1 eV. For the Pt/ $\text{Ti}_{0.9}\text{Ce}_{0.1}\text{O}_2$  catalyst the peak can be deconvoluted in two contributions, the one at higher binding energies attributed to  $\text{Ti}^{4+}$  with good interaction with  $\text{Ce}^{4+}$ , also demonstrated by Francisco et al. and Stakheev et al. [18,19], respectively.

Fig. S2 also contains the O 1s spectra for all the samples. In the spectral deconvolution, the first peak at lower binding ener-

Table 5

XPS analysis results for reduced catalysts.

Reduced catalysts	Ti/Ce (XPS)	Ti 2 $p_{3/2}$ BE (eV)	Ce(III)%	% O 1s B	Pt/(Ti + Ce)
Pt/ $\text{TiO}_2$	–	459.3	–	9.68	0.0632
Pt/ $\text{Ti}_{0.98}\text{Ce}_{0.02}\text{O}_2$	16.81	458.7	49.62	10.36	0.0222
Pt/ $\text{Ti}_{0.9}\text{Ce}_{0.1}\text{O}_2$	5.21	458.4, 459.5	53.07	12.80	0.0182
Pt/ $\text{Ti}_{0.5}\text{Ce}_{0.5}\text{O}_2$	0.47	458.5	36.16	8.80	0.0478
Pt/ $\text{Ti}_{0.2}\text{Ce}_{0.8}\text{O}_2$	0.04	458.2	35.78	24.48	0.0250
Pt/ $\text{CeO}_2$	–	–	39.92	12.07	0.0096



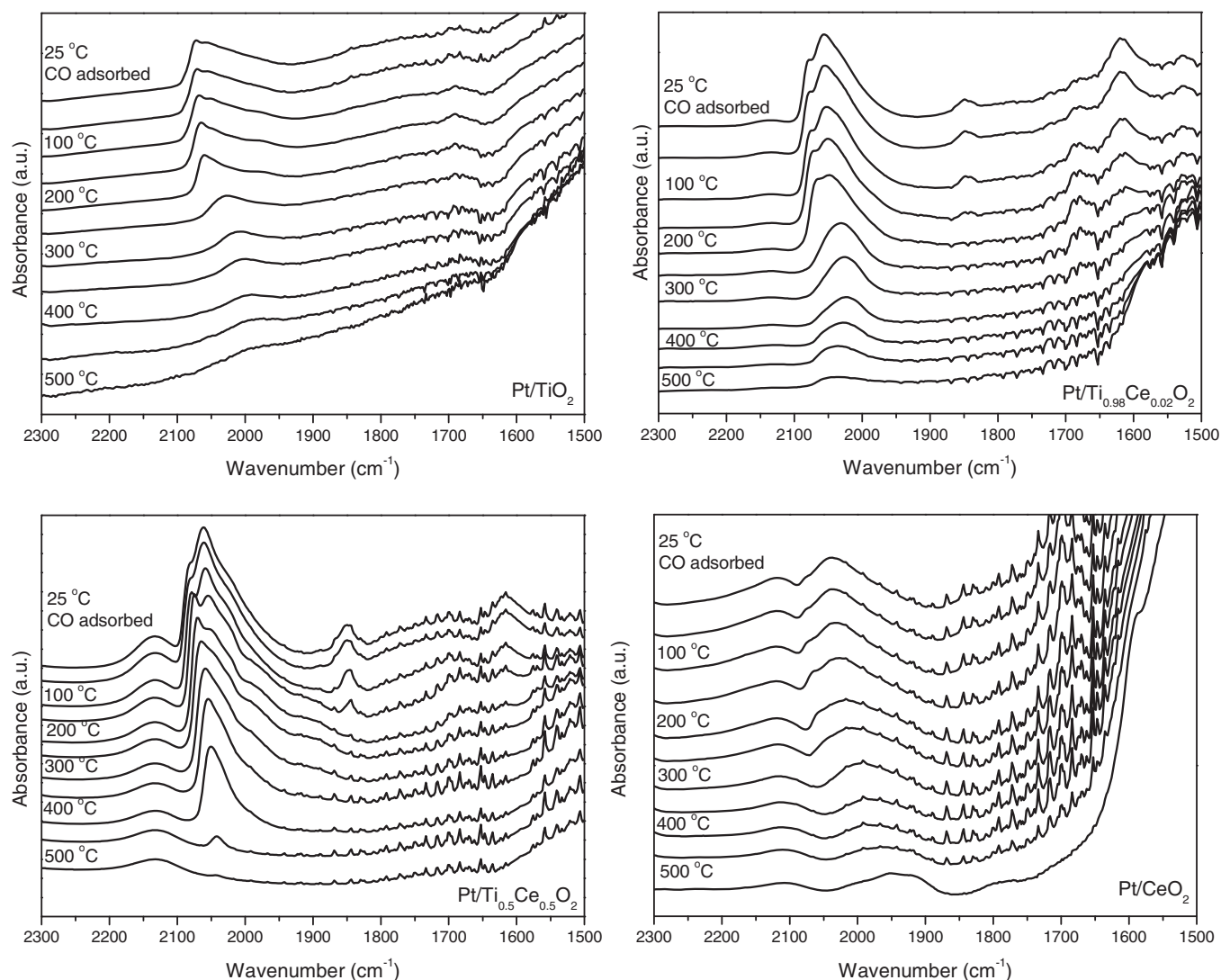


Fig. 6. DRIFTS analysis of some catalysts after CO adsorption increasing temperature. Spectra were taken every 50 °C.

gies is ascribed to lattice oxygen (O 1s A: O<sup>2-</sup> bonded to Ti or Ce cations) [20]. The second peak at higher binding energies is ascribed to mobile oxygen (O 1s B: hydroxyl groups, oxygen close to the vacancies) [21,22]. The binding energy shifts to lower values when cerium is added.

Table 5 shows the percentage of Ce(III) for all the samples, calculated by analyzing the Ce 3d core level [23]. In general, a decrease in ceria (by titania addition) produces initially a decrease in the percentage of Ce(III) up to  $x=0.5$ . Then, at lower ceria concentration, an increase in Ce(III) is detected.

### 3.7. Infrared spectroscopy of CO chemisorption

Platinum surface species were characterized by IR spectroscopy of chemisorbed CO. Fig. 6 reports the spectra recorded on the catalysts exposed to CO and subsequent desorption at increasing temperatures. CO adsorbed on Pt/TiO<sub>2</sub> shows two  $\nu(\text{CO})$  bands centered at 2073 and 2056 cm<sup>-1</sup> which are assigned to linear adsorption, while samples containing ceria show different features at 2057, 2079 and 2131 cm<sup>-1</sup> [24]. CO bridged exhibits a band between 1860 and 1870 cm<sup>-1</sup>. The samples behave differently upon heat treatment. Thus, for Pt/TiO<sub>2</sub> the peak centered at 2073 cm<sup>-1</sup> disappears after evacuation at 250 °C, while the peak centered at 2056 cm<sup>-1</sup> cannot be removed even at 500 °C, in spite

of a shift to lower wavenumbers. The peak at 2079 cm<sup>-1</sup>, shown in the samples containing ceria, is removed at different temperatures; thus, for sample Pt/Ti<sub>0.98</sub>Ce<sub>0.02</sub>O<sub>2</sub> the peak disappears at 250 °C, for Pt/Ti<sub>0.5</sub>Ce<sub>0.5</sub>O<sub>2</sub> at 200 °C. When ceria is added, a new peak develops at 2131 cm<sup>-1</sup> for all the ceria containing samples.

### 3.8. Catalytic activity

Two different catalytic experiments were carried out in this study. In the first one, the catalysts were tested in the reaction in a range of temperatures between 30 and 200 °C. The catalysts that showed a good activity at the PEMFC temperature (80 °C) were submitted to an isothermal reaction at this temperature in order to identify the best performing system. This last isothermal study is fully described in the supporting information (Catalyst stability: Figs. S6 and S7).

Fig. 7 shows that Pt/TiO<sub>2</sub> is the least active catalyst. Conversion at low temperatures increases when ceria is added. A big difference in CO conversion is clearly seen when the ceria fractional amount changes from 0.02 to 0.1 and following 0.5. At around 80 °C, the PEMFC working temperature, it is to be noted that the best performance is obtained with the catalysts supported on the mixed oxides with the highest ceria content ( $x=0.5$  and 0.2), which are even better than that of the Pt/CeO<sub>2</sub> catalyst. This emphasizes the

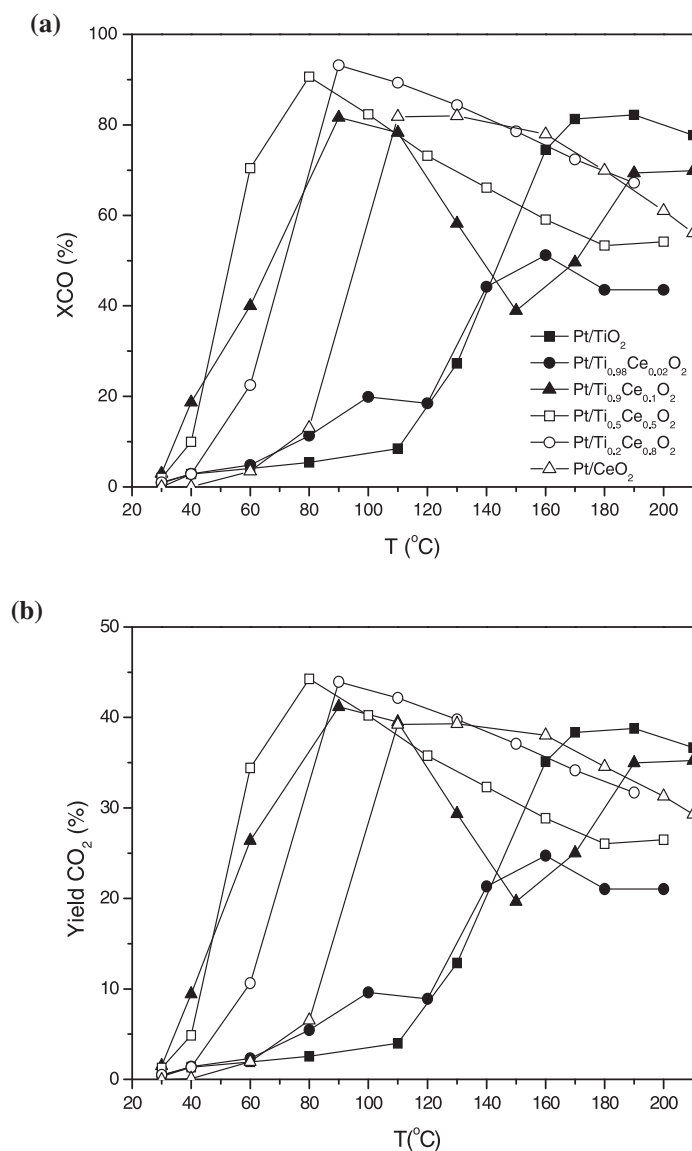


**Fig. 7.** PROX reaction on the Pt/Ti<sub>x</sub>Ce<sub>(1-x)</sub>O<sub>2</sub> catalysts between 30 and 200 °C: (a) CO conversion (%); (b) CO<sub>2</sub> yield (%).

importance of both components, ceria and titania, in the proper ratio.

### 3.8.1. Increase of H<sub>2</sub> concentration and addition of H<sub>2</sub>O and CO<sub>2</sub>

Finally, in order to simulate more realistic conditions, the effects of different feed compositions were studied. The H<sub>2</sub> concentration in the feed was increased, and H<sub>2</sub>O and CO<sub>2</sub> were added. All the above-mentioned components are present in a real flow after the reforming unit, so the desired catalyst must maintain its behavior in the presence of these contaminants. In the initial experiment, 5% CO<sub>2</sub> and 5% H<sub>2</sub>O were added to the feed mixture (Fig. 8). The tendency shown by the catalysts is similar to that observed in the absence of carbon dioxide and water; maintaining the temperature of maximum conversion but decreasing the conversion values, being more different at temperatures above 90 °C. Next, the percentage of H<sub>2</sub> was increased until 70%, and also water and CO<sub>2</sub> were added. A slight decrease in conversion with H<sub>2</sub> addition is suffered due to competitive adsorption, but taking into account that addition of water and CO<sub>2</sub> do not produce a noticeable effect. Isothermal experiments (shown in Supporting information Fig. S7) proved the stability of the catalyst under different conditions (ideal,

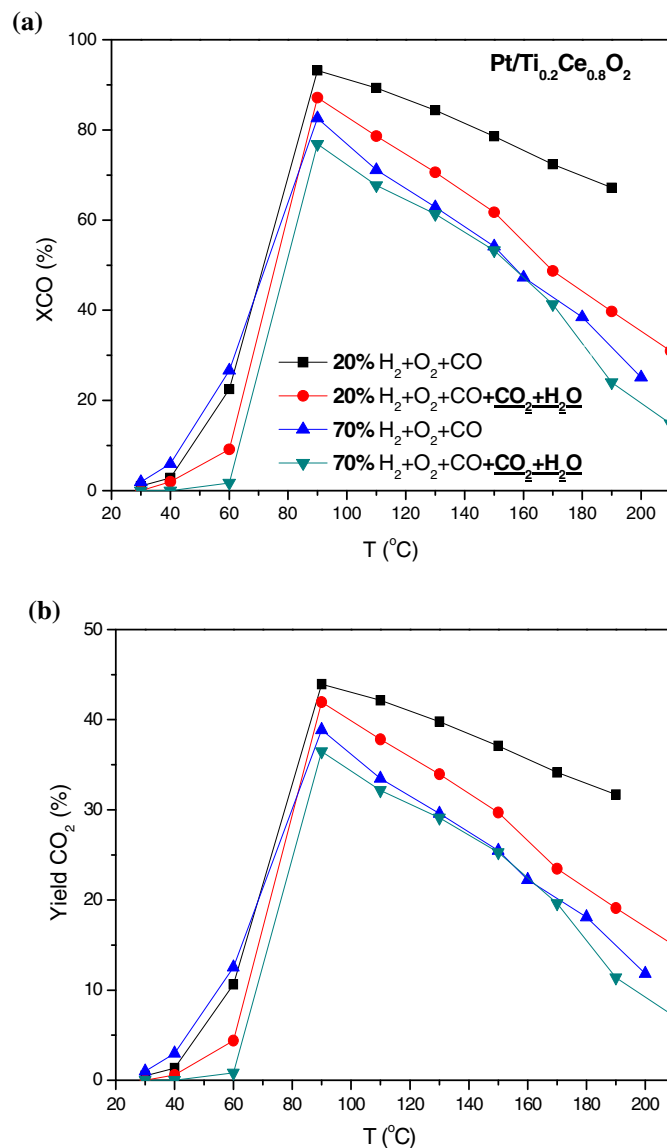


**Fig. 8.** CO conversion (%) and CO<sub>2</sub> yield (%) for the most active sample (Pt/Ti<sub>0.2</sub>Ce<sub>0.8</sub>O<sub>2</sub>) under ideal and real conditions, water and CO<sub>2</sub> in the feed stream.

H<sub>2</sub> addition and also adding CO<sub>2</sub> and water); no clear deactivation is observed when H<sub>2</sub>O and CO<sub>2</sub> are added. In fact, the conversion increases with time due to a possible removal of adsorbed surface species.

## 4. Discussion

### 4.1. Characterization

Table 1 shows that the nominal composition of the catalysts is very similar to the experimental one, while the addition of dopants affects the porous texture (Table 2). Ceria addition strongly increases the surface area, which goes from <10 m<sup>2</sup> g<sup>-1</sup> in pure TiO<sub>2</sub> to 100 m<sup>2</sup> g<sup>-1</sup> for pure CeO<sub>2</sub> [18,21,25]. The surface area is high enough to accommodate the desired amount of platinum nanoparticles. When doped mixed oxide materials are used, the efficient formation of the desired solid solution should be proven, since different scenarios may be at hand: (i) a physical mixture of both metal oxides, (ii) cerium is replacing titanium atoms in the TiO<sub>2</sub> phases, (iii) titanium atoms are replacing cerium atoms in the ceria fluorite structure, (iv) a combination of the above mentioned sce-

narios. XRD shows significant differences between samples. Pure  $\text{TiO}_2$  is present in the form of anatase and rutile phases, as it could be expected. When ceria is added, the anatase characteristic peaks decrease with increasing amount of cerium. They also broaden and slightly shift toward larger angles, which points to the formation of a solid solution [21]. Taking into account that rutile is the most stable crystalline  $\text{TiO}_2$  phase, the transformation of anatase into rutile is inhibited (rutile peaks almost disappear) in the presence of  $\text{CeO}_2$ , as it can be seen in the XRD patterns [26]. Lin and Yu justified this fact by the formation of Ti–O–rare earth bonds; at the interface, an interaction between different structures inhibits the phase transformation [27]. This points to the formation of a solid solution for the mixed oxide supports. Focusing in the X-ray spectra of supports  $x = 0.98$  and  $0.9$ , a new broad peak at  $30.7^\circ$  appears. Luo et al. attributed this band to a new monoclinic phase formed by ceria substitution in the titania framework [26]. Shen et al.'s results suggested a real chemical reaction yielding  $\text{Ce}_2\text{TiO}_5$  [28].

When ceria concentration reaches 50%, the peaks of the cubic fluorite structure appear, and it is important to remark that they are shifted toward higher  $2\theta$  with respect to pure ceria. This also indicates that the fluorite lattice is modified, probably due to the substitution of titanium atoms in the ceria lattice. When the concentration of ceria increases, the fluorite peaks gradually shift toward lower angle values. X-ray diffractograms have also been determined for samples after platinum impregnation and after reaction (Fig. S1). It can be seen that the diffraction patterns do not change significantly, proving the stability of these materials.

The formation of a solid solution is far from being trivial since, if the crystallinity is not good enough, a simple XRD analysis might fail. In order to ensure the presence of such solid solution, Raman spectroscopy was utilized. In this case, the detection of the pure phases present in the supports should be possible by looking at their specific Raman modes, and will not be related to the crystallinity. Fig. 3(a) shows the Raman spectra of all the samples. It is important to remark that the  $\text{TiO}_2$  active mode  $E_g$  is shown for all the samples containing  $\text{TiO}_2$ , even in the samples that do not show anatase peaks in the XRD pattern. The evolution of the anatase phase in the  $\text{TiO}_2$  nanocrystals can be well characterized by the change of the lowest-frequency  $E_g$  Raman mode with a decrease in  $\text{TiO}_2$  content. A combined mechanism involving phonon confinement and non-stoichiometry effects might be proposed. It means that the  $\text{TiO}_2$  particle size decreases and the number of defects in the anatase phase increases [29]. These results, together with XRD, reveal that anatase phase of titania is modified by the presence of ceria because of the substitution of Ti atoms with cerium atoms. As cerium is added, the appearance of the symmetric breathing mode of cerium ( $F_{2g} \sim 464 \text{ cm}^{-1}$ ) is observed (Fig. 3(c)), which is in agreement with XRD results showed above. For samples with low ceria content, the ceria Raman modes do not appear, this pointing to cerium atoms being just incorporated in the  $\text{TiO}_2$  lattice. When the concentration of ceria reaches 50%, the peak  $F_{2g}$  appeared. This peak is broader and slightly blue shifted with respect to the pure ceria sample. These results also suggest that part of the cerium atoms are being replaced by Ti atoms. Summarizing, XRD and Raman spectroscopy clearly showed the formation of solid solutions for all the samples studied.

At this stage, it is important to analyze the structure–property relationships of the synthesized catalysts. UV–vis spectra in Fig. 4 show a change in absorption with the composition. Thus, pure  $\text{TiO}_2$  and  $\text{CeO}_2$  show very similar spectra with an absorption band centered at 400 nm, very much in agreement with results found in literature [30,31]. The mixed oxides showed different behavior: the absorption band is shifted to higher wavelengths when the concentration of  $\text{CeO}_2$  increases up to 50%, then the absorption band shifted toward lower wavelengths. It is clear that the formation of a solid solution strongly modified the optical and

electronic properties of the supports. We tentatively explain this shift with respect to the pure oxides as follows:  $\text{CeO}_2$  defect-free is an insulator with a band gap of 6 eV (absorption at  $\sim 200 \text{ nm}$ ), the valence and conduction bands resulting from O 2p and Ce 5d states, respectively. Between these two bands, it appears a flat Ce 4f band which is 2 eV below the Fermi level. For pure  $\text{CeO}_2$  the latter band is empty, but it can become partially occupied if  $\text{Ce}^{3+}$  is present in the structure or by the incorporation of  $\text{Ti}^{4+}$  in the ceria lattice [32]. In short, the incorporation of Ti in the ceria lattice produces absorption enhancement at the visible light range. It happens up to certain concentration, and then the absorption band of  $\text{TiO}_2$  becomes predominant. This technique demonstrates the change in the electronic properties of the prepared supports; it may also have an important impact in the redox properties of the catalyst.

The catalyst reducibility has been assessed by TPR experiments. All profiles (Fig. 5), except that corresponding to the pure titania-supported catalyst, show two peaks: a sharp one at low temperature and a broader one at high temperature. The one at low temperature shifts toward higher temperatures when the concentration of ceria increases. This peak is assigned to the reduction of platinum particles and support in close contact with the platinum particles, due to spillover phenomenon [33]. Indeed, ceria addition hampers the reduction of the support at low temperatures. The extent of reduction, calculated by quantifying the  $\text{H}_2$  consumption (Table 4), increases with the ceria content up to  $x = 0.5$ , after which it decreases. The amount of hydrogen consumed correlates very well with the position of the absorption band measured by UV. Thus, the sample that has the absorption band located at the highest wavelengths is the sample that consumes more hydrogen.

The results obtained with XPS and CO chemisorption give information about surface properties of the different catalysts. First, a shift to lower binding energies in the Ti  $2p_{3/2}$  spectra (obviously of the catalysts containing Ti) is observed upon increasing the concentration of ceria (Fig. S2). The latter may be related to the partial reduction of  $\text{Ti}^{4+}$ – $\text{Ti}^{3+}$  or to the incorporation of cerium in the titania lattice. If we consider that cerium (1.5 Pauling units) is less electronegative than titanium (1.1 Pauling units), the substitution of titanium atoms by cerium in the titania lattice will produce an enhanced electron density on Ti, and consequently, a decrease in binding energy [34].

When the Ce 3d core level (Fig. S3) is considered, six peaks corresponding to the three pairs of spin–orbit doublets of Ce(IV) and two peaks corresponding to the doublet of Ce(III) are observed. Explanation of the origin of each doublet is given in detail in the work by Burroughs et al. [35]. The analysis of the peaks can be used to quantify the percentage of Ce(III) at the surface. However, the measurement of this percentage implies an intrinsic error, since  $\text{Ce}^{4+}$  can easily be reduced to  $\text{Ce}^{3+}$  during the measurement. Therefore, we could not find a direct correlation between the  $\text{Ce}^{3+}/\text{Ce}^{4+}$  atomic ratio and concentration of Ce in the catalysts [17,36–39]. However, it is important to remark that all catalysts containing cerium contain more than 35% of  $\text{Ce}^{3+}$ .

When looking at the Pt 4f level (see Fig. S4) different Pt species, from  $\text{Pt}^{4+}$  to  $\text{Pt}^{2+}$  can be observed [40]. All these XPS results indicate that the catalysts have a remarkable redox nature, since all their constituents are present in different oxidation states. The analysis of the location of the orbitals responsible for the redox properties with respect to the Fermi level can prove this latter statement. From literature and from our own experiments (Fig. S5) we know that the Ce 4f lies  $\sim 2 \text{ eV}$  below the Fermi level, as it can be deduced from the valence band of the  $\text{Ce}_2\text{O}_3$  [32]. For  $\text{Ce}^{4+}$  this level is empty [17]. Something similar happens with the Ti 3d band, for  $\text{Ti}^{4+}$  is empty and located  $\sim 1.5 \text{ eV}$  below the Fermi level. It is also known that oxidic platinum species have electron density at level Pt 5d very close to the Fermi level. It means that the Ti 3d, Ce 4f and Pt 5d levels overlap at below the Fermi level; consequently, any change



in oxidation state of one of the catalyst component will modify the oxidation state of the other components, resulting in a material that may be considered a redox buffer [17,41–43].

Apart from the oxidation state, surface composition of the catalysts can also be extracted from XPS results. When comparing the Ti/Ce atomic ratios calculated by XPS (surface technique) and XRF (bulk technique), the values differs, indicating a ceria surface segregation. This is interesting since, when other metals were used to create mixed oxides with ceria, the second metal oxide tends to segregate to the surface [4,44] in our system happens the contrary.

The Pt/(Ce + Ti) atomic ratios calculated by XPS can be considered an indication of Pt dispersion [45]. According to Table 5, the Pt/(Ce + Ti) atomic ratio increases with the concentration of ceria until  $x=0.5$  is reached, then the ratio decreases. The pure titania sample shows a very high value compared to the other samples. The Pt dispersion calculated by CO chemisorption follows the same trend as the XPS results, with the exception of the pure titania sample (Table 1).

Fig. 6 shows the IR spectra measured during adsorption of CO for four samples: Pt/CeO<sub>2</sub>, Pt/TiO<sub>2</sub>, Pt/Ti<sub>0.98</sub>Ce<sub>0.02</sub>O<sub>2</sub> and Pt/Ti<sub>0.5</sub>Ce<sub>0.5</sub>O<sub>2</sub>. For all samples with the exception of Pt/TiO<sub>2</sub> a band  $\nu(\text{CO})$  above 2100 cm<sup>-1</sup> assigned to CO adsorbed on oxidized platinum species or strongly interacting with the support is observed [24]. At lower wavenumbers a broad band that can be deconvoluted in several peaks for all samples, including Pt/TiO<sub>2</sub>, and assigned to linearly adsorbed CO in different reduced Pt sites is observed. Surprisingly, the strength of CO adsorbed on oxidized Pt is relatively high, disappearing only upon thermal treatment at 500 °C. For the Pt/Ti<sub>0.5</sub>Ce<sub>0.5</sub>O<sub>2</sub> sample this band disappears even at a higher temperature than the one of CO adsorbed on reduced Pt. This fact suggests that oxidized Pt or interacting with the support must be crucial in the oxidation of CO [46].

#### 4.2. Catalytic performance

The catalysts were tested in the PROX reaction. Fig. 7 shows the light off curves for all catalysts. In all cases CO conversion increases with temperature until it reaches a maximum and H<sub>2</sub> oxidation takes place. An optimum yield to CO<sub>2</sub> is achieved at 80 °C (Fig. 7b), which is the working temperature of PEMFC. Catalytic performance of ceria containing samples is better than for the pure oxides. When these results are compared in terms of TOF (Table 1), a similar trend is observed. Shape of the light off curve for catalyst Pt/Ti<sub>0.9</sub>Ce<sub>0.1</sub>O<sub>2</sub> can be explained by formation of superficial groups which block the surface and make the conversion decreases between 80 and 150 °C. Increasing temperature, hydroxyl, carbonate groups or even water adsorbed produced as a secondary products are removed, and conversion gives a rise.

#### 4.3. Structure–performance relationships and plausible reaction mechanism

Fig. 9 shows the conversion of CO conversion at 80 °C as a function of the composition of the supports. We can see that there is a broad range of supports compositions in which the CO conversion at 80 °C is maximized. The secondary y-axis shows absorption band values obtained from the UV–vis analysis. Both graphs nicely match, inferring an important correlation between the electronic properties of the support and the catalyst performance. On the other hand, these changes in the electronic properties of the supports are well in line with the reducibility of the support. Furthermore, DRIFTS experiments showed that CO is strongly adsorbed on oxidized Pt species or Pt in close interaction with the support.

Taking into account these results we can propose a plausible reaction mechanism based on redox cycles, which is schematized in Fig. 10. Thus, CO is first adsorbed on oxidized Pt species; then CO

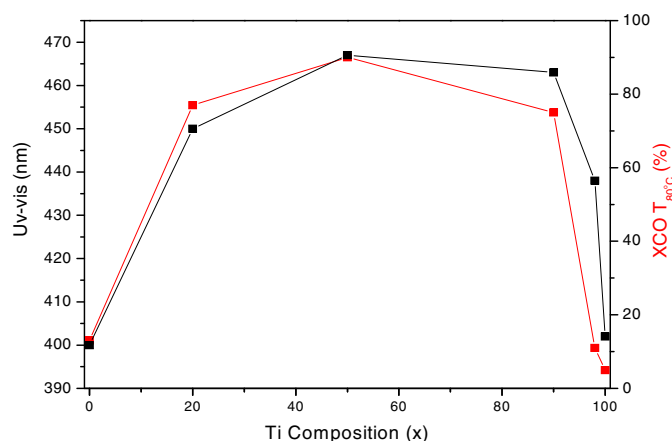


Fig. 9. UV–vis and X<sub>CO</sub> at 80 °C versus support content of Ti.

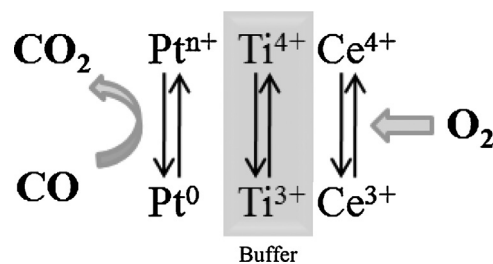


Fig. 10. Proposed reaction mechanism for PROX reaction over the synthesized materials.

is oxidized there and Pt is reduced to Pt<sup>0</sup>. From the valence band structure analysis we know that Pt 5d is closer to the empty Ti 3d level than to the empty Ce 4f level. It means that Ti<sup>4+</sup> will be reduced to Ti<sup>3+</sup> with the consequent oxidation of Pt<sup>0</sup>. In other words, it will be very likely for the electron to go from the Pt 5d to the Ti 3d band. The next step should be the regeneration of the Ti<sup>3+</sup>, which can be done by direct oxidation with oxygen present in the reaction mixture (following a classical Mars van Krevelen mechanism [3]) or by another redox cycle. In this new cycle Ti<sup>3+</sup> is oxidized to Ti<sup>4+</sup> by reduction of Ce<sup>4+</sup>–Ce<sup>3+</sup> (“two-steps Mars van Krevelen mechanism”). The latter is very likely because the empty band of Ce 4f is very close to the partially occupied Ti 3d band of Ti<sup>3+</sup>. Finally, oxygen in the reaction mixture regenerates Ce<sup>3+</sup>.

The proposed “two-steps Mars van Krevelen mechanism” is more effective for PROX reaction than the one-step one. It can be explained in the following way: in the presence of only TiO<sub>2</sub>, the rate-limiting step is oxygen activation, this because Ti<sup>3+</sup> is more difficult to regenerate than Ce<sup>3+</sup> [47]. On the other extreme, in case of Pt/CeO<sub>2</sub>, the rate-limiting step is the regeneration of Pt to oxidized Pt. This is because the Pt 5d band is closer to Ti 3d than to the one of Ce 4f.

Finally, the oxidation of H<sub>2</sub> follows a similar path. However, it is well known from the literature that H<sub>2</sub> chemisorbs better on Pt<sup>0</sup> than on Pt<sup>δ+</sup> at low temperatures [48–53], indeed in the TPR profiles, hydrogen consumption is always above 80 °C for all samples. Once this temperature at which the Pt<sup>δ+</sup> species may be reduced, H<sub>2</sub> is preferentially oxidized.

## 5. Conclusions

Structure–activity relationships in Pt supported on Ti<sub>x</sub>Ce<sub>(1-x)</sub>O<sub>2</sub> solids were investigated for a series of Ti<sub>x</sub>Ce<sub>(1-x)</sub>O<sub>2</sub> ( $x = 1, 0.98, 0.9, 0.5, 0.2$  and 0) supports prepared by sol–gel. The resulting catalysts after impregnation of Pt were characterized in detail by applying a

wide range of techniques and tested in the preferential oxidation of CO in the presence of H<sub>2</sub>.

For the studied reaction, a strong correlation between catalyst performance and the electronic properties of the supports has been found. Support reducibility and the overlap of Pt 5f, Ce 4f and Ti 3d levels at the valence band seem to be crucial parameters that determine catalytic performance. These results have been rationalized on the basis of a redox cascade mechanism.

## Acknowledgments

Financial support from Generalitat Valenciana and Ministerio de Economía y Competitividad (Spain) through projects PROMETEOII/2014/004 and MAT2010-21147 is gratefully acknowledged. EOJ also thanks the CNPq – Brazil for her grant. EVRF gratefully acknowledge the Ministerio de Economía y Competitividad (Spain) for his Ramon y Cajal grant (RYC-2012-11427).

## Appendix A. Supplementary data

Supplementary data associated with this article can be found, in the online version, at <http://dx.doi.org/10.1016/j.apcatb.2015.06.031>

## References

- [1] A. Kulprathipanja, G.O. Alptekin, J.L. Falconer, J.D. Way, *Ind. Eng. Chem. Res.* 43 (2004) 4188.
- [2] V.M. Lebarbier, R.A. Dagle, L. Kovarik, K.O. Albrecht, X. Li, L. Li, C.E. Taylor, X. Bao, Y. Wang, *Appl. Catal. B: Environ.* 144 (2014) 223.
- [3] F. Mariño, C. Descorme, D. Duprez, *Appl. Catal. B: Environ.* 58 (2005) 175.
- [4] I. Atribak, B. Azambre, A. Bueno López, A. García-García, *Appl. Catal. B: Environ.* 92 (2009) 126.
- [5] Q. Yu, L. Liu, L. Dong, D. Li, B. Liu, F. Gao, K. Sun, L. Dong, Y. Chen, *Appl. Catal. B: Environ.* 96 (2010) 350.
- [6] A. Naumenko, I. Gnatiuk, N. Smirnova, A. Eremenko, *Thin Solid Films* 520 (2012) 4541.
- [7] D.A. Shirley, *Phys. Rev. B* 5 (1972) 4709.
- [8] Y. Hu, H.L. Tsai, C.L. Huang, *J. Eur. Ceram. Soc.* 23 (2003) 691.
- [9] B. Choudhury, A. Choudhury, *Mater. Sci. Eng. B* 178 (2013) 794.
- [10] S. Yang, W. Zhu, Z. Jiang, Z. Chen, J. Wang, *Appl. Surf. Sci.* 252 (2006) 8499.
- [11] M. Thammachart, V. Meeyoo, T. Risksomboon, S. Osuwan, *Catal. Today* 68 (2001) 53.
- [12] E. Moretti, L. Storaro, A. Talon, M. Lenarda, P. Riello, R. Frattini, M.d.V.M. de Yuso, A. Jiménez-López, E. Rodríguez-Castellón, F. Ternero, *Appl. Catal. B: Environ.* 102 (2011) 627.
- [13] T. Ohsaka, F. Izumi, Y. Fujiki, *J. Raman Spectrosc.* 7 (1978) 321.
- [14] K.R. Zhu, M.S. Zhang, Q. Chen, Z. Yin, *Phys. Lett. A* 340 (2005) 220.
- [15] M.L. Dos Santos, R.C. Lima, C.S. Riccardi, R.L. Tranquilin, P.R. Bueno, J.A. Varela, E. Longo, *Mater. Lett.* 62 (2008) 4509.
- [16] X.M. Lin, L.P. Li, G.S. Li, W.H. Su, *Mater. Chem. Phys.* 69 (2001) 236.
- [17] T. Baidya, A. Gayen, M.S. Hegde, N. Ravishankar, L. Dupont, *J. Phys. Chem. B* 110 (2006) 5262.
- [18] M.S. Francisco, V.R. Mastelaro, P.A.P. Nascente, A.O. Florentino, *J. Phys. Chem. B* 105 (2001) 10515.
- [19] A.Y. Stakheev, E.S. Shpiro, J. Apijok, *J. Phys. Chem.* 97 (1993) 5668.
- [20] J. Fang, X. Bi, D. Si, Z. Jiang, W. Huang, *Appl. Surf. Sci.* 253 (2007) 8952.
- [21] D. Yu, Y. Liu, Z. Wu, *Catal. Commun.* 11 (2010) 788.
- [22] V.P. Santos, M.F.R. Pereira, J.J.M. Órfao, J.L. Figueiredo, *Appl. Catal. B: Environ.* 99 (2010) 353.
- [23] J. Silvestre-Albero, F. Rodríguez-Reinoso, A. Sepúlveda-Escribano, *J. Catal.* 210 (2002) 127.
- [24] M. Shen, L. Lv, J. Wang, J. Zhu, Y. Huang, J. Wang, *Chem. Eng. J.* 255 (2014) 40.
- [25] A. Martínez-Arias, M. Fernández-García, L.N. Salamanca, R.X. Valenzuela, J.C. Conesa, J. Soria, *J. Phys. Chem. B* 104 (2000) 4038.
- [26] M. Luo, J. Chen, L. Chen, J. Lu, Z. Feng, C. Li, *Chem. Mater.* 13 (2000) 197.
- [27] J. Lin, J.C. Yu, *J. Photochem. Photobiol. A* 116 (1998) 63.
- [28] Y. Shen, D. Zheng, B. Yang, S. Ni, S. Zhu, *J. Rare Earths* 30 (2012) 431.
- [29] H. Yoshitake, D. Abe, *Micropor. Mesopor. Mater.* 119 (2009) 267.
- [30] S. Kundu, J. Ciston, S.D. Senanayake, D.A. Arena, E. Fujita, D. Stacchiola, L. Barrio, R.M. Navarro, J.L.G. Fierro, J.A. Rodríguez, *J. Phys. Chem. C* 116 (2012) 14062.
- [31] M. Gonzalez Castañón, T.R. Reina, S. Ivanova, M.A. Centeno, J.A. Odriozola, *J. Catal.* 314 (2014) 1.
- [32] D.D. Sarma, M.S. Hegde, C.N.R. Rao, *J. Chem. Soc. Faraday Trans. 2* 77 (1981) 1509.
- [33] A. Trovarelli, *Catalysis by Ceria and Related Materials*, Imperial College Press, London, 2002.
- [34] K.C. Petalidou, K. Polychronopoulou, S. Boghosian, S. Garcia-Rodriguez, A.M. Efsthathiou, *J. Phys. Chem. C* 117 (2013) 25467.
- [35] P. Burroughs, A. Hammett, A.F. Orchard, G. Thornton, *J. Chem. Soc. Dalton Trans.* 17 (1976) 1686.
- [36] E.O. Jardim, S. Rico-Francés, F. Coloma, J.A. Anderson, E.V. Ramos-Fernandez, J. Silvestre-Albero, A. Sepúlveda-Escribano, *Appl. Catal. A: Gen.* 492 (2015) 201.
- [37] E.O. Jardim, S. Rico-Francés, F. Coloma, E.V. Ramos-Fernández, J. Silvestre-Albero, A. Sepúlveda-Escribano, *Appl. Catal. A: Gen.* 487 (2014) 119.
- [38] E. Ramos-Fernández, J. Serrano-Ruiz, J. Silvestre-Albero, A. Sepúlveda-Escribano, F. Rodríguez-Reinoso, *J. Mater. Sci.* 43 (2008) 1525.
- [39] J.C. Serrano-Ruiz, E.V. Ramos-Fernández, J. Silvestre-Albero, A. Sepúlveda-Escribano, F. Rodríguez-Reinoso, *Mater. Res. Bull.* 43 (2008) 1850.
- [40] E.V. Ramos-Fernández, B. Samaranich, P. Ramírez de la Piscina, N. Homs, J.L.G. Fierro, F. Rodríguez-Reinoso, A. Sepúlveda-Escribano, *Appl. Catal. A: Gen.* 349 (2008) 165.
- [41] D. A. Andersson, I. Simak, V. Skorodumova, I. A. Abrikosov, B. Johansson, *Appl. Phys. Lett.* 90 (2007).
- [42] T. López, F. Rojas, R. Alexander-Katz, F. Galindo, A. Balankin, A. Buljan, *J. Solid State Chem.* 177 (2004) 1873.
- [43] G. Zhou, J. Hanson, R.J. Gorte, *Appl. Catal. A: Gen.* 335 (2008) 153.
- [44] E.V. Ramos-Fernandez, N.R. Shiju, G. Rothenberg, *RSC Adv.* 4 (2014) 16456.
- [45] F.P.J.M. Kerkhof, J.A. Moulijn, *J. Phys. Chem.* 83 (1979) 1612.
- [46] O. Pozdnyakova, D. Teschner, A. Wootsch, J. Kröhnert, B. Steinhauer, H. Sauer, L. Toth, F.C. Jentoft, A. Knop-Gericke, Z. Paál, *J. Catal.* 237 (2006) 1.
- [47] Z. Wu, H. Zhu, Z. Qin, H. Wang, L. Huang, J. Wang, *Appl. Catal. B: Environ.* 98 (2010) 204.
- [48] E.P.J. Mallens, J.H.B.J. Hoebink, G.B. Marin, *Catal. Lett.* 33 (1995) 291.
- [49] E.V. Ramos-Fernandez, C. Pieters, B. van der Linden, J. Juan-Alcañiz, P. Serra-Crespo, M.W.G.M. Verhoeven, H. Niemantsverdriet, J. Gascon, F. Kapteijn, *J. Catal.* 289 (2012) 42.
- [50] E.V. Ramos-Fernández, A. Sepúlveda-Escribano, F. Rodríguez-Reinoso, *Catal. Commun.* 9 (2008) 1243.
- [51] E.V. Ramos-Fernández, A.F.P. Ferreira, A. Sepúlveda-Escribano, F. Kapteijn, F. Rodríguez-Reinoso, *J. Catal.* 258 (2008) 52.
- [52] E.V. Ramos-Fernández, J.M. Ramos-Fernández, M. Martínez-Escandell, A. Sepúlveda-Escribano, F. Rodríguez-Reinoso, *Catal. Lett.* 133 (2009) 267.
- [53] E.V. Ramos-Fernández, J. Ruiz-Martínez, J.C. Serrano-Ruiz, J. Silvestre-Albero, A. Sepúlveda-Escribano, F. Rodríguez-Reinoso, *Appl. Catal. A: Gen.* 402 (2011) 50.